Fast Multiparametric Electromagnetic Full-Wave Inversion via Solving Contracting Scattering Data Equations Optimized by the 3-D MRF Model

Yanjin Chen, Jiawen Li, Jianliang Zhuo, Feng Han, *Senior Member, IEEE,* and Qing Huo Liu, *Fellow, IEEE*

***Abstract*— This article presents a novel hybrid electromagnetic full-wave inversion that combines the traditional inversion method, i.e., the variational Born iterative method (VBIM), with the 3-D Markov random field (MRF) model. In each iteration, VBIM first reconstructs the model parameters of all discretized cells in the inversion domain by solving the discretized data equations. Then, MRF is adopted to classify the cells according to the reconstructed parameter values, i.e. to determine which homogenous scatterer a certain cell is belonging to. Finally, partial cells classified as "background" are removed, and partial cells classified as "scatterer" are merged. Consequently, the discretized data equations gradually contract, and the unknowns in the following VBIM iterations are reduced. Numerical experiments show that compared with the traditional VBIM, the proposed hybrid VBIM-MRF model can achieve higher reconstruction accuracy for multiple model parameters. Furthermore, the computational cost is also significantly reduced.**

***Index Terms*— Electromagnetic scattering, full-wave inversion, Markov random field (MRF), variational Born iterative method (VBIM).**

I. INTRODUCTION

ELECTROMAGNETIC (EM) inversion techniques and their applications have developed rapidly in the past decades due to the fast increase of computer speed and memory and the development of fast forward modeling methods. The general purpose of EM inversion is to retrieve the model parameters, such as shapes, locations, or constitutive parameters of unknown objects in a specific region by using the scattered field data measured at the receiver arrays located outside that region. The applications mainly include radar imaging of moving targets [1], breast cancer diagnostics [2], microwave imaging of concealed weapons for security check [3], subsurface nondestructive testing [4], controlled-source electromagnetic detection [5], geophysical logging [6], and so on.

Three kinds of physical phenomena occur when the EM wave impinges on the unknown targets. They are geometric spreading, energy absorption, and scattering. The popular but rigorous method to formulate the interaction between the EM waves and the targets is using the state equation (also known as the Lippmann–Schwinger equation [7]) and the data equation. Unfortunately, the state and data equations are nonlinear and ill-posed for the target parameters. Solving them iteratively usually leads to high computational costs [7]. Several simplified or approximation approaches have been proposed to invert for the model parameters of unknown targets with low costs.

The first kind is utilizing the geometric spreading of the high-frequency waves to locate the positions or boundaries of unknown targets, which is often referred to as migration or focusing. For example, the reverse time migration (RTM) is widely employed in subsurface detection [8] by the ground-penetrating radar (GPR). The basic idea of RTM is to emit the reversed reflected wave pulses recorded at the receiver positions back to the inversion domain. Because the incident and reversed reflected waveforms are well correlated in the timestamps corresponding to spatial positions of the targets, autofocusing images emerge near the targets in the inversion domain. Another commonly used method to find the geometric shapes and boundaries of the targets is the linear sampling method (LSM) [9], [10] that actually is to cast the measured EM fields at the receiver arrays into the far-field spherical symmetrical waves radiated by a focusing point source in the inversion domain. More sophisticated methods to reconstruct the supports of the unknown targets include the direct sampling method (DSM) [11] and the orthogonality sampling method (OSM) [12]. They have the implementation processes similar to that of LSM but can produce the target images with lower costs or higher accuracy.

The second kind is utilizing the wave propagation delay or amplitude attenuation inside the unknown targets, which is often referred to as tomography and is widely applied for medical imaging [13]. If the measured phase or attenuation of the EM waves at the receivers can be approximately treated as a linear function of the geometry and inhomogeneous dielectric constants of targets, the backprojection (BP) tomography is usually adopted to estimate the dielectric parameter distribution of the whole inversion domain [14]. However, it is

---

Manuscript received February 29, 2020; revised April 24, 2020 and June 23, 2020; accepted July 20, 2020. Date of publication August 19, 2020; date of current version November 4, 2020. This work was supported in part by the National Key Research and Development Program of the Ministry of Science and Technology of China under Grant 2018YFF01013300. *(Corresponding author: Feng Han.)*

Yanjin Chen, Jiawen Li, Jianliang Zhuo, and Feng Han are with the Institute of Electromagnetics and Acoustics, Key Laboratory of Electromagnetic Wave Science and Detection Technology, Xiamen University, Xiamen 361005, China (e-mail: feng.han@xmu.edu.cn).

Qing Huo Liu is with the Department of Electrical and Computer Engineering, Duke University, Durham, NC 27708 USA (e-mail:qhliu@duke.edu).

Color versions of one or more of the figures in this article are available online at http://ieeexplore.ieee.org.

Digital Object Identifier 10.1109/TMTT.2020.3015518

assumed that the EM wave propagates such as straight-line rays in the projection tomography. For low-frequency EM waves, the diffraction tomography (DT) is preferred since the diffraction effect of the EM waves surrounding the targets is accounted for by the DT. The DT methods include the Born and Rytov approximations [15] and so on.

The first kind of method only reconstructs the general positions and shapes of the targets, but the dielectric parameters are not available. Although the BP and BA can be used to invert for the dielectric parameters, they are only valid for the weak scattering scenarios. Therefore, the rigorous full-wave inversion is necessary to solve the state and data equations to obtain both the geometric and dielectric parameters of the scatterers with high contrasts and/or large electrical dimensions. Due to the nonlinearity and ill-posedness of the EM inverse scattering problems, a cost function with the additive regularization or multiplicative terms is constructed to transform the inverse problem into an optimization problem. Several iterative methods, such as distorted iterated virtual experiments (DIVE) [16], the Born iterative method (BIM) and its variants, contrast source inversion (CSI), and the subspace optimization method (SOM), have been proposed to minimize the cost function. BIM starts from the Born approximation and solves the state and data equations alternately until the mismatch between the measured scattered field data and predicted field data reaches a stop criterion [17], [18]. The variational BIM (VBIM) [19] and distorted BIM (DBIM) [18] are implemented similarly, but the differential variables of model parameters are updated in the inverse computation. Different from BIM, CSI has no forward computation. The cost function includes the mismatches of both the data and state equations. The induced current and dielectric contrasts in the inversion domain are updated alternately until the total mismatch reaches the minimum [20]. SOM is similar to CSI, but the optimization is implemented in a subspace of the induced current [21].

Although the deep learning techniques advanced in recent years [22], [23] can overcome the time-consuming iterations, offline training is inevitable before implementing the online full-wave inversion. In addition, the deep learning scheme is usually model-dependent, i.e., the neural network must be trained again once the inversion model is changed. The disadvantage of the iterative method is that it suffers from the unaffordable computational burden for electrically large problems, which becomes more severe for the voxel-based 3-D inversion in which there are usually a huge number of unknowns in the discretized data equations.

In this article, we propose a hybrid full-wave inversion method that has the merits of the traditional iterative methods but can significantly lower the computational cost. It is assumed that the background medium inside the inversion domain is homogeneous, and inhomogeneous scatterers can be divided into several homogeneous subscatterers. After the whole inversion domain is discretized, many cells share the same dielectric parameters since both the background medium and scatterers always take several discretized cells. However, in the traditional iterative methods, the dielectric parameters of all the discretized cells are solved independently. If we can make use of the *a priori* information that many discretized cells in the inversion domain share the same dielectric parameters and merge the unknowns of these cells in the discretized data equations, the computational cost can be reduced correspondingly. Noting that the reconstructed 3-D model parameter distribution inside the inversion domain is analogous to a pixel-based image and each homogeneous scatterer or subscatterer is similar to an object embedded in the background, we segment the 3-D image reconstructed by the traditional iterative method using the Markov random field (MRF) model [24]. Because VBIM converges faster than BIM but has no need to update the Green's functions as in the DBM, it is selected and combined with the MRF model in this article. In each iteration, the reconstructed model parameters by VBIM in all the cells in the inversion domain are classified by the MRF model. Several cells belonging to a certain homogeneous scatterer or subscatterer or to the background medium with high fidelity will be merged in the discretized data equations. The merged cells belonging to the background medium will be completely removed in the next VBIM iteration since the equivalent current in the "background" cells is null. Here, the word "merge" means that the unknowns for all these cells in the discretized data equations are kept the same, and the corresponding row vectors in the Fréchet derivative matrix are added together. The word "remove" means that the unknowns in the "background" cells will be discarded in the discretized data equations, and the corresponding row vectors in the Fréchet derivative matrix are deleted. In this way, the discretized data equation gradually contracts as the VBIM iterations continue, and thus, the computational cost is reduced. Although the MRF model was also adopted in the Bayesian framework for nonlinear inverse scattering in previous works [25], [26], the implementation is quite different from that in our work. In [25], the maximum *a posteriori* (MAP) of the permittivity contrast was iteratively solved by stochastic approaches. However, in our work, the MRF and MAP are only used to classify the cells. The contrasts of the model parameters are actually solved the deterministic method VBIM. In [26], the contrasts were completely estimated by the joint MAP. Both the deterministic and stochastic solvers were discarded. Another popular method in the Bayesian framework used for inverse scattering is compressive sensing (CS). For example, in [27] and [28], the Bayesian CS was employed to image sparse dielectric profiles. In [29], nonweak and extended scatterers were also reconstructed using CS by incorporating the sparsity of contrast gradient.

In our work, the MRF model is embedded inside the iterations of the deterministic method VBIM. The organization of this article is given as follows. In Section II, the forward model and the inversion model for electromagnetic scattering are briefly described. Then, the MRF and its hybridization with VBIM are presented in detail. In Section III, two numerical examples are used to verify the proposed hybrid method. The first one is used to validate the feasibility and efficiency of VBIM-MRF. The second one is to test its adaptability to anisotropic scatterers and the antinoise ability. Finally, in Section IV, the conclusion, discussions, and future work are presented.

II. METHODS

In this section, the forward and inverse scattering formulas are briefly described in the framework of volume integral equations. In addition, the hybridization of VBIM and MRF models is discussed in detail.

A. Forward Model

If the layered background medium is uniaxial anisotropic and the scatterers embedded in a certain layer are fully anisotropic, the state equations (Lippmann–Schwinger equations) used to formulate the forward scattering are expressed as

$$\begin{aligned}\mathbf{E}^n_{\text{inc}}(\mathbf{r}) &= \mathbf{E}^n_{\text{tot}}(\mathbf{r}) - \mathbf{E}^n_{\text{sct}}(\mathbf{r})\\ &= \overline{\overline{\epsilon}}^{-1}(\mathbf{r})\frac{\mathbf{D}^n_{\text{tot}}(\mathbf{r})}{\varepsilon_0}\\ &\quad - j\omega\int_D \overline{\overline{\mathbf{G}}}{}^{nm}_{\mathbf{EJ}}(\mathbf{r},\mathbf{r}')\cdot\overline{\overline{\chi}}_{\epsilon}(\mathbf{r}')\mathbf{D}^m_{\text{tot}}(\mathbf{r}')d\mathbf{r}'\\ &\quad - j\omega\int_D \overline{\overline{\mathbf{G}}}{}^{nm}_{\mathbf{EM}}(\mathbf{r},\mathbf{r}')\cdot\overline{\overline{\chi}}_{\mu}(\mathbf{r}')\mathbf{B}^m_{\text{tot}}(\mathbf{r}')d\mathbf{r}' \quad (1\text{a})\\ \mathbf{H}^n_{\text{inc}}(\mathbf{r}) &= \mathbf{H}^n_{\text{tot}}(\mathbf{r}) - \mathbf{H}^n_{\text{sct}}(\mathbf{r})\\ &= \overline{\overline{\mu}}^{-1}(\mathbf{r})\frac{\mathbf{B}^n_{\text{tot}}(\mathbf{r})}{\mu_0}\\ &\quad - j\omega\int_D \overline{\overline{\mathbf{G}}}{}^{nm}_{\mathbf{HJ}}(\mathbf{r},\mathbf{r}')\cdot\overline{\overline{\chi}}_{\epsilon}(\mathbf{r}')\mathbf{D}^m_{\text{tot}}(\mathbf{r}')d\mathbf{r}'\\ &\quad - j\omega\int_D \overline{\overline{\mathbf{G}}}{}^{nm}_{\mathbf{HM}}(\mathbf{r},\mathbf{r}')\cdot\overline{\overline{\chi}}_{\mu}(\mathbf{r}')\mathbf{B}^m_{\text{tot}}(\mathbf{r}')d\mathbf{r}' \quad (1\text{b})\end{aligned}$$

where $\mathbf{E}^n_{\text{inc}}$ and $\mathbf{H}^n_{\text{inc}}$ are the incident fields evaluated in the nth layer when the scatterers are absent. $\mathbf{D}^n_{\text{tot}}$ and $\mathbf{B}^n_{\text{tot}}$ are the total flux densities in the nth layer when the scatterers are present in the inversion domain D. $\overline{\overline{\mathbf{G}}}{}^{nm}_{\mathbf{EJ}}$, $\overline{\overline{\mathbf{G}}}{}^{nm}_{\mathbf{EM}}$, $\overline{\overline{\mathbf{G}}}{}^{nm}_{\mathbf{HJ}}$, and $\overline{\overline{\mathbf{G}}}{}^{nm}_{\mathbf{HM}}$ are the dyadic Green's functions of uniaxial layered media [30] linking scatterers in the mth layer and field values in the nth layer. Equation (1) is valid for the anisotropic magnetodielectric scattering scenario but can be easily simplified to isotropic scattering formulas, and their weak forms can be found in [31], [32]. In the forward scattering computation, we let $n = m$ and (1) is discretized, and the total fields $\mathbf{D}^m_{\text{tot}}$ and $\mathbf{B}^m_{\text{tot}}$ are solved by the stabilized biconjugate-gradient fast Fourier transform (BCGS-FFT) [32].

B. Inversion Model

The inverse scattering is formulated by the data equations that can be expressed as

$$\begin{aligned}\mathbf{E}^n_{\text{sct}}(\mathbf{r}) &= j\omega\int_D \overline{\overline{\mathbf{G}}}{}^{nm}_{\mathbf{EJ}}(\mathbf{r},\mathbf{r}')\cdot\overline{\overline{\chi}}_{\epsilon}(\mathbf{r}')\mathbf{D}^m_{\text{tot}}(\mathbf{r}')d\mathbf{r}'\\ &\quad + j\omega\int_D \overline{\overline{\mathbf{G}}}{}^{nm}_{\mathbf{EM}}(\mathbf{r},\mathbf{r}')\cdot\overline{\overline{\chi}}_{\mu}(\mathbf{r}')\mathbf{B}^m_{\text{tot}}(\mathbf{r}')d\mathbf{r}' \quad (2\text{a})\\ \mathbf{H}^n_{\text{sct}}(\mathbf{r}) &= j\omega\int_D \overline{\overline{\mathbf{G}}}{}^{nm}_{\mathbf{HJ}}(\mathbf{r},\mathbf{r}')\cdot\overline{\overline{\chi}}_{\epsilon}(\mathbf{r}')\mathbf{D}^m_{\text{tot}}(\mathbf{r}')d\mathbf{r}'\\ &\quad + j\omega\int_D \overline{\overline{\mathbf{G}}}{}^{nm}_{\mathbf{HM}}(\mathbf{r},\mathbf{r}')\cdot\overline{\overline{\chi}}_{\mu}(\mathbf{r}')\mathbf{B}^m_{\text{tot}}(\mathbf{r}')d\mathbf{r}' \quad (2\text{b})\end{aligned}$$

where $\mathbf{E}^n_{\text{sct}}$ and $\mathbf{H}^n_{\text{sct}}$ are the scattered fields measured at the receiver arrays in the nth layer. In the inverse scattering computation, (2) is discretized, and the contrast $\overline{\overline{\chi}}$ is solved by VBIM [19], [33]. The cost function with the regularization term in the $(k+1)$th iteration is constructed as

$$\mathbf{F}_{k+1} = \frac{\|\delta\mathbf{f}_k - \mathbf{A}\delta\mathbf{y}_{k+1}\|^2}{\|\delta\mathbf{f}_k\|^2} + \gamma^2\frac{\|\delta\mathbf{y}_{k+1}\|^2}{\|\delta\mathbf{y}_k\|^2} \quad (3)$$

where $\delta\mathbf{f}_k$ is the difference between the measured scattered fields at the receiver arrays and the predicted scattered fields in the kth iteration, the vector $\mathbf{y}$ is composed of the contrasts of all the unknown dielectric parameters for all the discretized cells in the inversion domain, $\mathbf{A}$ is the Fréchet derivative matrix, γ^2 is the regularization factor, and $\|\|$ denotes the L_2 norm. In the conventional BCGS-FFT-VBIM, (1) and (2) are solved alternately, and thus, the total fields and contrasts are updated alternately until the misfits of measured scattered fields and predicted values reach a stop criterion. The conjugate gradient (CG) method is used to solve (3). One should note that the dimensions of $\mathbf{A}$ and $\mathbf{y}$ keep unchanged in all the iteration steps in the previous works [18], [19], [33], [34], which usually leads to a high computational cost for 3-D inversion problems.

C. MRF Algorithms Applied to VBIM Results

As mentioned in Section I, the reconstructed model parameter values in all the discretized cells of the whole inversion domain are similar to the gray values of pixels of a 3-D image. The MRF model, which has been successfully applied to image segmentation [35], can be adapted to divide the discretized cells into "scatterer" ones and "background" ones. As shown in the previous works [19], [33], [34], [36], the VBIM can obtain the model parameter values in all the cells although they may be inaccurate at the beginning of the iterations. However, neighboring cells usually have close reconstructed model parameters. In other words, "scatterer" cells tend to cluster together to form a subregion or several subregions, and "background" cells tend to cluster together to form the subregion of the background medium. The MRF is a probabilistic model that is good at capturing such contextual constraints [37]. We assume that there are $N = N_x \times N_y \times N_z$ discretized cells and $K-1$ homogeneous scatterers or subscatterers with different model parameters embedded in the homogeneous background medium, i.e., there are K kinds of different media. According to the Hammersley–Clifford theorem [37], the MRF model is equivalent to the Gibbs distribution [38] that can be compactly written as

$$P(x_i = k) = \frac{\exp\left(-\sum_{c\in C} V_c(x_i = k)\right)}{\sum_{k=1}^{K}\exp\left(-\sum_{c\in C} V_c(x_i = k)\right)} \quad (4)$$

where i is the index of the discretized cell, k is the index of the medium kind, and $P(x_i = k)$ is the probability of the ith cell being judged as the kth kind of medium. V_c is the potential of the clique c, and C is the gather of all cliques [39]. Because we are dealing with 3-D images, the third neighbors of a clique are adopted in this article, as shown in Fig. 1. In other words, there are 26 cells surrounding the cell whose medium kind will be determined using (4). For a practical 3-D image, the evaluation of (4) can be simply and intuitively

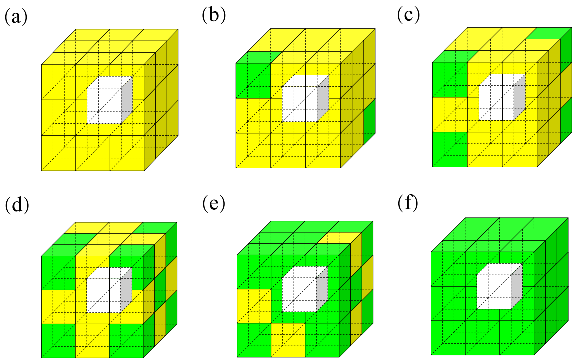

Fig. 1. Third neighbors in the MRF model. The medium kind of the cell with the white color in the center is to be determined. The cells with the green color are the "scatterer" cells, while those with the yellow color are the "background" cells. There are 0, 2, 4, 8, 21, and 26 "scatterer" cells surrounding the cell with the white color in (a)–(f), respectively.

replaced [40] by computing the ratio of the total number of cells belonging to a certain medium kind with respect to the total number: 26. As shown in Fig. 1, if there are two kinds of media, e.g., the homogeneous scatterer and the homogeneous background, the probability for the cell in the center being judged as the "scatterer" is 0 in (a), (2/26) in (b), (4/26) in (c), (8/26) in (d), (21/26) in (e), and 1.0 in (f), respectively.

Once the probability of the classification of the ith cell is evaluated, the probability of the model parameter of that cell can be computed by

$$P(y_i|x_i = k) = \frac{1}{\sqrt{2\pi}\sigma_k}\exp\left(-\frac{(y_i-\mu_k)^2}{2\sigma_k^2}\right) \tag{5}$$

where y_i is the model parameter, e.g., relative permittivity or conductivity, in the ith cell, and μ_k and σ_k are the mean and the variance of the model parameter, respectively, supposing that the ith cell is classified as the kth kind of medium. Then, the final classification (or the medium kind) of the ith cell can be determined using the MAP

$$\begin{aligned}\widehat{x_i} &= \arg\max_{1\leq k\leq K}\ P(x_i = k|y_i)\\ &= \arg\max_{1\leq k\leq K}\ \frac{P(y_i|x_i = k)P(x_i = k)}{P(y_i)}.\end{aligned} \tag{6}$$

Since the denominator of (6) is a constant, $\widehat{x_i}$ can be evaluated readily using results of (4) and (5).

Four points must be mentioned here.

1) The conditional probability of the model parameter is described by the Gaussian distribution given in (5). Such a choice is reasonable. Because the 3-D voxel-based electromagnetic inversion problem is usually ill-posed and the discretized data equations are always underdetermined, the model parameters in all discretized cells solved by VBIM are pseudorandom [41]. According to the central limit theorem of the statistics, the reconstructed model parameters in the discretized cells belonging to each homogeneous subregion of the inversion domain will automatically follow the Gaussian distribution.
2) The mean μ_k and variance σ_k are obtained by the maximum likelihood estimate (MLE) from the sample cells that are determined belonging to the same homogeneous subregion.
3) If the number of model parameter kinds is more than one, e.g., when both relative permittivity and conductivity are reconstructed or anisotropic scatterers are considered, the multivariate Gaussian distribution is used to replace (5).
4) The evaluation of (4)–(6) must be performed iteratively until the classifications (or medium kinds) of all the discretized cells remain unchanged. The reason is that the classification of a discretized cell is unknown at the beginning although the VBIM can reconstruct all the model parameters of all the cells.

Thus, the medium kind for each cell is chosen randomly at the beginning, and it is finally determined by solving (4)–(6) several times. The detailed procedure of this iteration can be found in the flowchart shown in Fig. 2.

D. Hybridization of VBIM and MRF Models

Fig. 2 shows the flowchart of the hybridization of VBIM and the MRF model. The whole process includes three steps.

1) Step I—VBIM: The traditional VBIM is implemented to reconstruct the model parameters of the discretized cells in the inversion domain. The details of BCGS-FFT-VBIM have been presented in our previous work [34] and will not be repeated here.

2) Step II—Classification: The MRF model is used to classify the discretized cells in the inversion domain, i.e., to determine the medium kind of each cell. As emphasized in Section II-C, this is an iterative process. First, we randomly choose the medium kind of each cell and solve (4). Then, the MLE is used to obtain the mean and variance in (5), and the probability of the model parameter is computed. Finally, the classification for each cell is determined based on (6). These three sequential steps are repeated several times until the classifications for all cells remain unchanged. This iterative process is shown in the second part of Fig. 2.

3) Step III—Merging: Once the medium kind of each cell is obtained by the MRF classification, partial cells will be merged. Such an operation is reasonable because it is unnecessary to reconstruct the model parameters of two discretized cells independently if they belong to the same medium kind. However, the MRF is a statistical model. It is unreliable to merge all the cells judged as the same class. Therefore, an empirical threshold is used to select the cells with high fidelity, which will be merged. For the "background" cells, the ith cell satisfying the following condition

$$d_i = \frac{|y_i - y_b|}{\max\limits_{1\leqslant n\leqslant N}(|y_n - y_b|)} < \mathrm{th1} \tag{7}$$

will be merged. Here, y_b is the true parameter of the background medium, and $th1$ is a user-defined threshold that is less than 1. Equation (7) implies that only the cells with their reconstructed model parameters close enough to the true background model parameters will be merged. In addition, for multiple model parameters, e.g., both permittivity and conductivity or full tensors of arbitrary anisotropy, all model

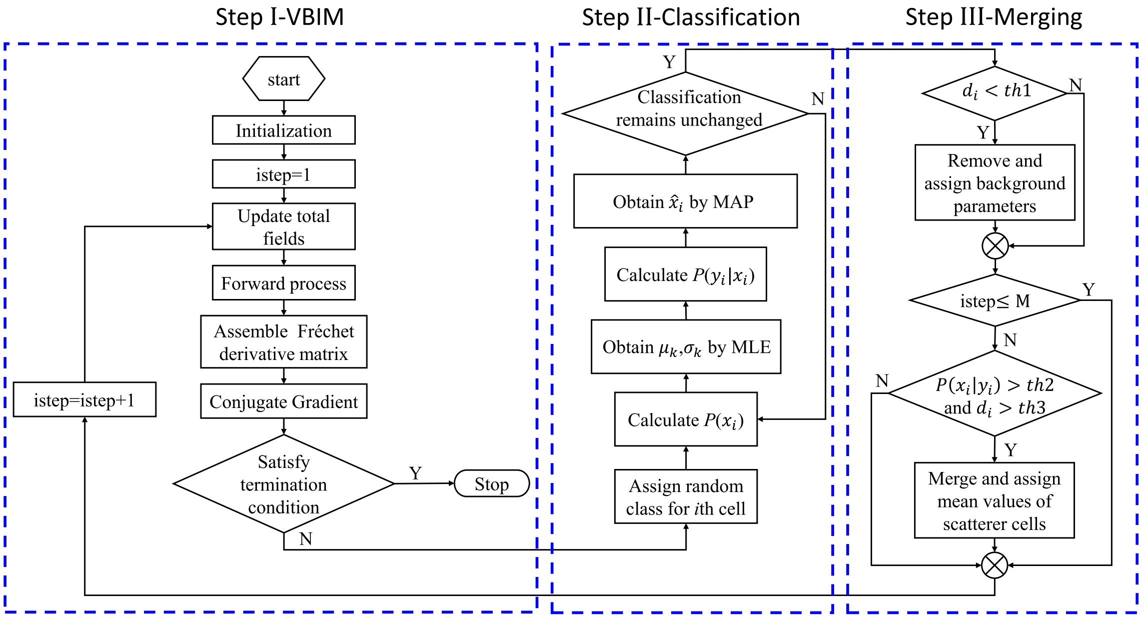

Fig. 2. Flowchart of the VBIM-MRF hybridization. In Step I, the VBIM is implemented to reconstruct the model parameters of all the discretized cells. In Step II, the MRF model is employed to iteratively classify the cells. In Step III, partial "background" cells and "scatterer" cells are merged, and thus, the dimensions of the vector **y** and the Fréchet derivative matrix **A** in (3) are reduced correspondingly. When Step III is complete, we need to go back to implement the VBIM again. The termination condition of the whole process is that there is no cell that can be merged in five successive iterations.

parameters must satisfy (7) simultaneously. Similarly, for the "scatterer" cells, the ith cell satisfying the following two conditions simultaneously

$$P(x_i = \text{“scatterer”}|y_i) > \text{th2} \tag{8a}$$

$$d_i > \text{th3} \tag{8b}$$

will be merged. Equation (8b) has a similar effect as (7) but selects the cells with their reconstructed model parameters far enough from the background model parameters. Equation (8a) helps to select the cells belonging to the "scatterer" medium with a high probability. One should note that the unknowns in the merged "background" cells will be completely removed from the vector **y**, and the corresponding rows in the Fréchet derivative matrix **A** in (3) are also deleted. This operation is valid since the equivalent current in the "background" cells is null and has no contribution to the measured scattered fields. Thus, the reconstructed model parameters of these removed "background" cells will be mandatorily assigned the known background medium parameters. By contrast, only one unknown is kept in the vector **y**, and the corresponding row vectors in the Fréchet derivative matrix **A** are added together for the merged "scatterer" cells. Such an operation is also reasonable since these cells are determined to belong to the same homogeneous scatterer and to have the same model parameters. The reconstructed model parameters of the kept cell are assigned as the mean values of all the merged cells. In addition, merging the "background" cells is performed in each iteration of VBIM. However, only after the pure VBIM is carried out M times, merging the "scatterer" cells begin. This is because VBIM only updates the variations of the unknowns in each iteration, and the initial model parameter values of all the cells are set the same as the background medium parameters. After the VBIM is performed enough times, the reconstructed model parameters of the scatterers approach the true values. At this stage, it is more reliable to merge the "scatterer" cells. The termination condition of the whole hybridization process is that there is no cell that can be merged in five successive iterations.

E. Comparisons With Other Methods

The proposed VBIM-MRF applies the MLE and MAP to VBIM results to obtain the classification of each discretized cell in the inversion domain. In each iteration, partial "background" cells are removed, and partial "scatterer" cells are merged. Consequently, the dimensions of both the unknown vector and the Fréchet derivative matrix in the discretized data equation are reduced. Comparisons of the proposed VBIM-MRF with other methods are analyzed in the following.

1) Comparison With VBIM: The hybrid VBIM-MRF outperforms the pure VBIM for both the reconstruction accuracy and implementation efficiency. Because the inversion domain is gradually compressed by the MRF algorithm in successive iterations of VBIM, the number of unknowns in the discretized data equation is reduced. However, the measured scattered field data remain unchanged. As a result, the ill-posedness of the inverse problem is actually mitigated. The VBIM becomes easier to find an optimized solution. On the other hand, both the time and memory consumption of VBIM-MRF are also lowered due to the compressed inversion domain. Of course, these advantages are only valid when VBIM-MRF can converge in each iteration, i.e., the three thresholds, $th1$, $th2$, and $th3$, in (7) and (8) are properly selected.

2) Comparison With Regularization: The MRF algorithm behaves like a regularization for the inverse problem since it also mitigates its ill-posedness. However, they are not the same since the goal is achieved in different ways. The MRF directly reduces the number of unknowns in the discretized data equation. However, the regularization is to add or multiply a penalty term to the cost function to mitigate the ill-posedness, e.g., the total variation (TV) used to capture sharp boundaries between the scatterers and the background medium [42]. The regularization reduces the searching space of the solutions through the additional penalty terms. However, the MRF realizes this purpose by deleting "background" cells or merging "scatterer" cells. Of course, because the MRF algorithm interferes with the convergence process of VBIM, the convergence curve of VBIM-MRF is not as smooth as that of the pure VBIM, which will be shown by the first numerical example in Section III.

3) Comparison With Iterative Multiscaling Approach: The proposed hybrid VBIM-MRF is similar to the iterative multiscaling approach (IMSA) proposed in [43] and [44] or the adaptive multiresolution technique given in [45] since the inversion domain is downsized iteratively for all these methods. However, they also show obvious differences. In VBIM-MRF, there is only one iterative loop for the full-wave inversion. If three thresholds, $th1$, $th2$, and $th3$, in (7) and (8) are chosen properly and VBIM-MRF can converge in each iteration and enter the next iteration, partial "background" cells will be removed, and thus, the inversion domain is gradually downsized. By contrast, in IMSA or the adaptive multiresolution technique, there are two nested loops. The outer loop is searching for the approximate locations of the scatterers, so as to reduce the inversion domain. The inner loop is the true full-wave inversion iteration. The discretization of the inversion domain is fixed in VBIM-MRF, while it is dynamically adjusted in the IMSA.

4) Comparison With Other Hybrid Methods: VBIM-MRF is different from the recently proposed hybrid method, i.e., VBIM-maximum entropy thresholding (MET) [46]. VBIM-MRF not only removes the "background" cells but also classifies all the homogeneous scatterers or subscatterers and merges the cells belonging to the same class. However, VBIM-MET only segments the "background" and "scatterer" subregions in the inversion domain. Two different homogeneous subscatterers inside one scatterer cannot be distinguished by VBIM-MET. VBIM-MRF is also different from the hybrid method presented in [47] since the MAP is employed in this article to judge the medium kind for each discretized cell. Another major difference is that only the "background" cells are removed by expectation maximization in [47]. The "scatterer" cells are not merged.

III. NUMERICAL RESULTS

In this section, we use two numerical examples to verify the proposed hybrid method. The background medium includes three layers. The top and bottom layers are air. The scatterers are embedded in the homogeneous middle layer. The transmitter and receiver arrays are placed in the top and bottom layers. In the first example, the scatterers are isotropic and homogeneous. In the second example, the scatterer is fully anisotropic and inhomogeneous. All the measured scattered field data are simulated by the BCGS-FFT solver. In both numerical experiments, three thresholds, $th1$, $th2$, and $th3$, in (7) and (8) are set as 0.4, 0.5, and 0.6, respectively. A larger $th1$ can accelerate the removal of the confirmed "background" cells, but some "scatterer" cells may be incorrectly deleted. As a result, the iteration of VBIM-MRF is not as stable as that of VBIM or even fails to converge. By contrast, a smaller $th1$ can guarantee the safety, but the discretized data equations also contract slower due to the slow removal of "background" cells. The thresholds $th2$ and $th3$ play similar roles for the contracting data equations by controlling the merging of the "scatterer" cells. Therefore, there is a tradeoff between the reliability and efficiency of VBIM-MRF implementation. Although the aforementioned three threshold values are empirical, the two numerical examples in this section will show that they can achieve a good balance between reliability and efficiency. The parameter M in the flowchart of Fig. 2 indicates the beginning merging step of the "scatterer" cells. It is set as 4 in the first numerical example but 10 in the second numerical example. Usually, more iterations of VBIM are necessary to reconstruct the preliminary profiles for anisotropic scatterers with multiple model parameters. Only when the reconstructed preliminary profiles of scatterers can be distinguished from the background medium in the inversion domain, merging the "scatterer" cells begins. If it starts too early, some "background" cells will also be merged into the scatterer. However, if it is too late, the merging almost becomes meaningless for the reduction of the computational cost of VBIM. In addition, in order to quantitatively evaluate the reconstruction performance of the proposed method, we use the data misfit and model misfit defined in [36, eqs. (16) and (17)]. The data misfit indicates how well the measured scattered fields match the predicted scattered fields in the iterations. The model misfit indicates how well the reconstructed model parameters match the true model parameters in the whole inversion domain. All the experiments are performed on a workstation with 20-core Xeon E2650 v3 2.3-GHz CPU, 512-GB RAM.

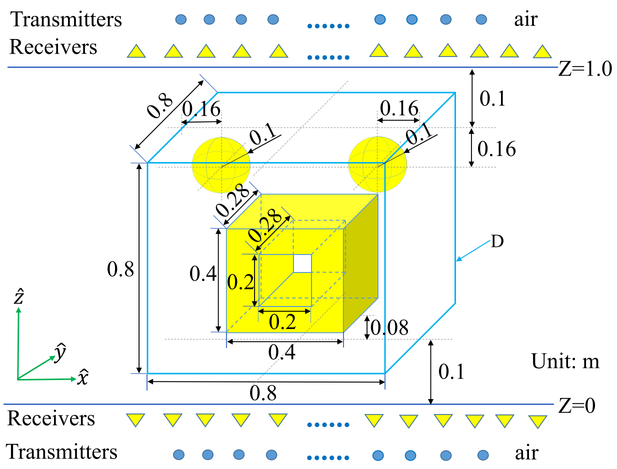

Fig. 3. Configuration of the inversion model with multiple homogeneous scatterers embedded in the middle layer.

A. Multiple Homogeneous Scatterers Embedded in the Middle Layer

1) Inversion Model Configuration: As shown in Fig. 3, there are three scatterers embedded in the middle layer. The radii of

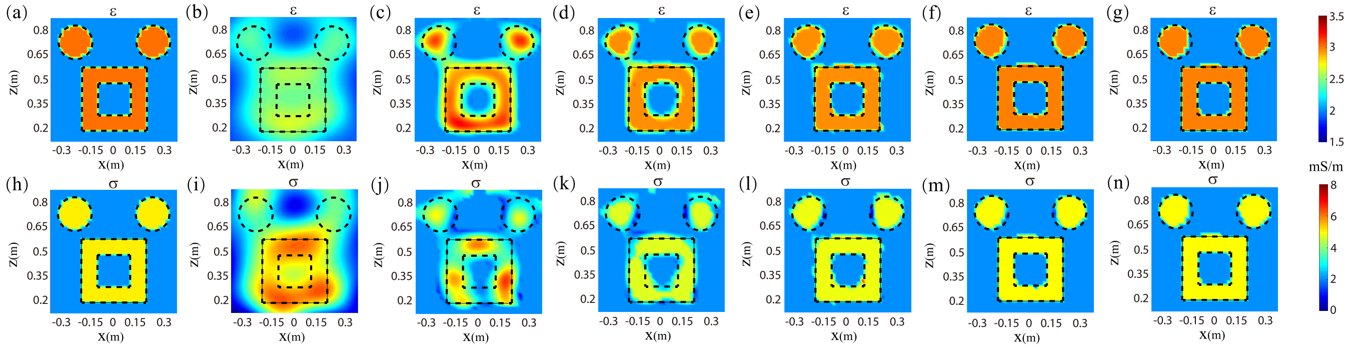

Fig. 4. Ground truth and reconstructed 2-D slices at $y = 0$ m in different iteration steps of VBIM. (a) and (h) Ground truth. (b)–(g) Inversion results of the relative permittivity in the first, third, fourth, sixth, 14th, and last steps. (i)–(n) Reconstructed conductivity in the same steps. Dotted lines: true shapes of scatterers.

two spheres are 0.1 m, and their centers are located at (−0.24, 0, 0.64) m and (0.24, 0, 0.64) m, respectively. The hollow cuboid has the dimensions of 0.4 m × 0.28 m × 0.4 m with its center located at (0, 0, 0.38) m. The size of the hole is 0.2 m × 0.28 m × 0.2 m. The dielectric parameters of three scatterers are the same. They are $\varepsilon = 3.0$ and $\sigma = 5$ mS/m. The inversion domain D has the dimensions of 0.8 m × 0.8 m × 0.8 m. Its center is located at (0, 0, 0.5) m and is divided into 40 × 40 × 40 cells. The size of each cell is $\Delta x = \Delta y = \Delta z = 0.02$ m. The dielectric parameters of the background medium are $\varepsilon = 2.0$ and $\sigma = 2$ mS/m. Thus, there are totally 128 000 unknowns to be reconstructed; 50 transmitters are uniformly located in two 2.4 m × 2.4 m planes at $z = -0.2$ m and $z = 1.2$ m, respectively. The operating frequency is 300 MHz. The scattered fields are collected by 72 receivers arrays uniformly located in two 4.0 m × 4.0 m planes at $z = -0.1$ m and $z = 1.1$ m, respectively. Thus, there are 43 200 data equations if we separate the real and imaginary parts of the scattered fields.

2) Downsizing the Inversion Domain: In each iteration, after the model parameters of all cells are reconstructed by VBIM, the MRF model is first used to classify the cells in the inversion domain. Then, partial confirmed "background" cells with high fidelity are merged and removed. Beginning in the fourth step, partial confirmed "scatterer" cells are also merged. Here, the word "confirmed" means the reconstructed model parameters in that cell satisfy (7) or (8). Fig. 4 shows the 2-D slices for the xz planes of the ground truth and the inversion results by VBIM-MRF in different iteration steps. In the full-wave inversion by VBIM, the initial model parameters of all cells in the inversion domain are assigned as the known background medium dielectric constants. Because the dielectric parameters of scatterers are different from the background medium parameters, it is inappropriate to merge the "scatterer" cells at the beginning of VBIM iterations. However, it is feasible to merge and remove the confirmed "background" cells at the beginning since the initial model parameters of all cells are the same as the background medium parameters. Therefore, in the first three steps, we only remove the "background" cells. As shown in Fig. 4(b) and (i), in the first step, the reconstructed model parameters of some "background" cells are close to the true parameters of the background medium, while the reconstructed parameters of "scatterer" cells are quite different from the true parameters. After some confirmed "background" cells are removed, the mean values of the "scatterer" cells gradually tend to be stable, as shown in Fig. 4(c) and (j). At this moment, we begin to merge "scatterer" cells, i.e., from the fourth step, the "background" cells are removed, and "scatterer" cells are merged synchronously. As shown in Fig. 4(d) and (k), because partial confirmed "scatterer" cells are merged, the distribution of the reconstructed model parameters in the scatterer subregion is more uniform. Furthermore, compared with the results in the third step, the structures of relative permittivity and conductivity of scatterers become more consistent. The poor inversion result of the conductivity shown in Fig. 4(j) is obviously improved. After the sixth step, most cells have been removed or merged, and only some cells locating near the boundaries between the scatterers and the background medium remain. As shown in Fig. 4(e)–(f) and (l)–(m), the inversion results after the 6th step do not change much. When no cell can be removed or merged in five consecutive steps, the termination condition is satisfied, and the whole hybridized process finishes. The final inversion results are shown in Fig. 4(g) and (n). It can be seen that the inversion results are very close to the ground truth. Meanwhile, the reconstructed model parameters of all discretized cells of the scatterers are the same due to the merging.

3) Classifying Discretized Cells: Fig. 5 shows the iterative process of MRF classification after the fourth-step VBIM outputs model parameter values in the discretized cells of the inversion domain. The first row shows the xz plane 2-D slices of the cell classes in different iterative steps. Blue indicates that the cell is classified as the background medium, while red indicates that the cell is classified as the scatterer. In other words, the label value of the background medium is 1, while it is 2 for the scatterer. The second row shows the value of $P(x_i = 1|y_i)$ in different iteration steps, while the third row shows the value of $P(x_i = 2|y_i)$ for the ith cell. In the beginning, we adopt the uniform distribution and randomly assign class labels to the reaming cells in the inversion domain, as shown in Fig. 5(b). As a result, $P(x_i = 1|y_i)$ and $P(x_i = 2|y_i)$ for the ith cell are equal to 0.5, as shown in Fig. 5(i) and (p). Because the MRF model incorporates the spatial connection of neighboring cells, the "scatterer" cells generated in the first step are

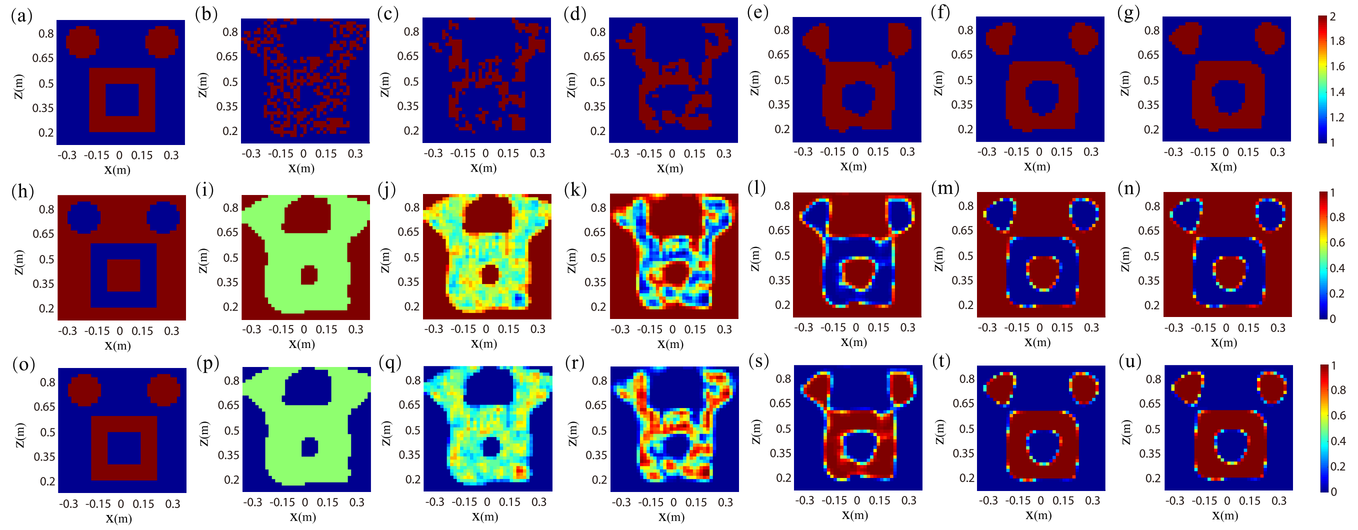

Fig. 5. 2-D slices at $y = 0$ m in different iterative steps of MRF classification for the fourth-step VBIM results. First row: MRF classification results. Second row: probability of cells belonging to the background. Third row: probability of cells belonging to scatterers. First column: ground truth. From the second column to the seventh column, they are for the first, second, third, fourth, eighth, and last steps of the iterations of the MRF classification.

gradually connected with others. Meanwhile, $P(x_i|y_i)$ also changes, as shown in Fig. 5(c), (g), and (q). Following this, the classification results are closer and closer to the ground truth with the iterations continue, as shown in Fig. 5(d)–(g). When the classifications for all the cells keep unchanged, the iteration stops. As can be seen in Fig. 5(n) and (u), the probability of most cells belonging to the scatterers is very close to 0 or 1, while the probability for cells located near the boundaries between scatterers and the background medium is different. There are two reasons for such a phenomenon. One is that the parameter values of the cells near the boundaries reconstructed by VBIM always fall between those of the background medium and the scatterers due to the L_2 norm cost function, which leads to $P(y_i|x_i = 2)$ and $P(y_i|x_i = 1)$ having close values. Second, because there is almost the same number of "background" cells and "scatterer" cells attached to the boundaries, $P(x_i = 2)$ and $P(x_i = 1)$ are also close.

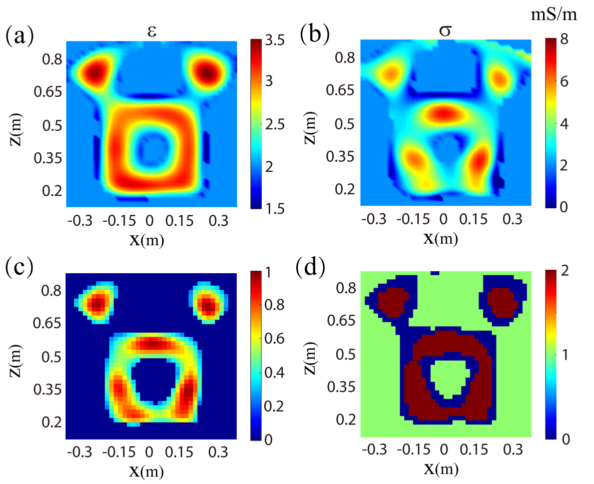

Fig. 6. Merging process illustrated by the 2-D xz slices at $y = 0$ m. The model parameters are reconstructed by VBIM in the fourth iteration. (a) Reconstructed relative permittivity. (b) Reconstructed conductivity. (c) Values of d_i in (7) and (8). (d) Cell merging results. The label value 2 denotes "scatterer," 1 denotes "background," and 0 denotes cell class to be determined.

4) Confirming Removed and Merged Cells: Once the MRF classification is finalized, i.e., the medium kind of each cell is determined, the operations of merging and removing will be implemented. Unfortunately, as shown in Fig. 4(c) and (j), the inversion results are not ideal in the early stages of VBIM iterations, and thus, directly removing "background" cells and merging "scatterer" cells determined by the MRF classification are not safe. Additional constraints are necessary. Only the "background" cells with the reconstructed model parameters satisfying the inequality in (7) will be removed. Only the "scatterer" cells with the reconstructed model parameters satisfying the inequalities in (8) will be merged. Fig. 6 shows the merging process applied to the reconstructed results by VBIM in the fourth iteration step. Fig. 6(a) and (b) shows the relative permittivity and conductivity reconstructed by VBIM. Fig. 6(c) shows the values of d_i in (7) and (8). By combing them with the probability values shown in Fig. 5(n) and (u), we can obtain the final merging results shown in Fig. 6(d). Red indicates that these "scatterer" cells have been merged, while green indicates that these cells have been removed. Blue indicates that these cells remain, and they will participate in the next VBIM iteration. Because only partial cells are removed or merged, the shape of the merging result shown in Fig. 6(d) is different from that of the classification result shown in Fig. 4(g).

5) Comparison of VBIM-MRF and VBIM: Fig. 7 shows the comparisons of reconstructed 3-D isosurfaces and profiles of relative permittivity and conductivity between VBIM-MRF and VBIM. It can be seen that the 3-D permittivity profiles reconstructed by VBIM are not distorted too much. However, the reconstructed conductivity profiles are poor. Fortunately, when the hybridized VBIM-MRF is employed, the structure consistency between permittivity and conductivity is mandatorily enforced through (5)–(8). As a result, the reconstructed shape is greatly improved. Meanwhile, due to the removal of the "background" cells and the merging of the "scatterer" cells,

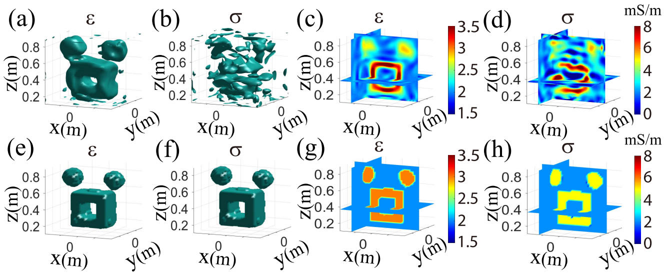

Fig. 7. Reconstructed 3-D isosurfaces and profiles of relative permittivity and conductivity. (a)–(d) By VBIM. (e)–(h) By VBIM-MRF.

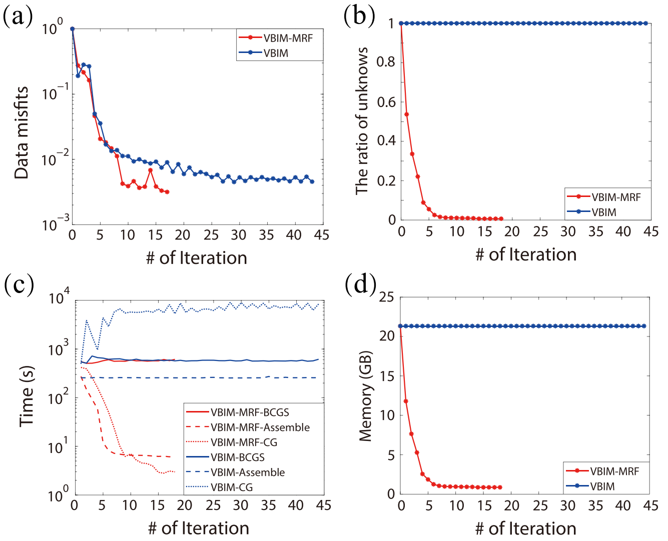

Fig. 8. Comparisons of the converging processes of VBIM and VBIM-MRF. (a) Variations of data misfits of the scattered fields in different iteration steps. (b) Ratio of unknowns in different iteration steps to the total unknowns in the first step. (c) Time consumed by BCGS, matrix assembly, and CG in different iteration steps. (d) Memory consumed in different steps.

the VBIM-MRF is able to reconstruct more precise model parameters compared with the conventional VBIM, as shown in Fig. 7(e)–(h).

Fig. 8(a) shows the variations of data misfits of the scattered fields in each iteration step. We can see that VBIM-MRF converges faster than VBIM but not as stable as VBIM. This is because the discretized cells are merged and the inversion domain is mandatorily changed in the iterations of VBIM-MRF. Fig. 8(b) shows the variations of the remaining cells in the computation domain in each iteration step. As can be seen, for VBIM-MRF, the number of unknowns decreases quickly in the first six steps. After this, it changes slowly. This is because most “background” cells have been removed and most “scatterer” cells have been merged in the first six steps. By contrast, for VBIM, the cell number keeps unchanged in the whole iteration process. Therefore, the discretized data equations of (2) gradually contract in the iterations of VBIM-MRF. Fig. 8(c) shows the time spent by the most time-consuming parts (BCGS, assembling the Fréchet derivative matrix and CG) in each iteration step. Due to the decrease in the number of unknowns, except for BCGS that has nothing to do with the number of unknowns, the computational time of assembling the Fréchet derivative matrix and CG is less in VBIM-MRF compared with those in VBIM. Furthermore, due to the poor reconstructed conductivity profile by VBIM [see Fig. 7(d)], the time consumption of CG in VBIM shows an upward trend. Fig. 8(d) shows the variations of memory consumption in each iteration step. Because the memory consumption is approximately in direct proportion to the number of unknowns of the discretized data equations, the overall trends of memory consumption are the same as those shown (b). Memory consumption of VBIM-MRF decreases rapidly, while that of VBIM keeps unchanged.

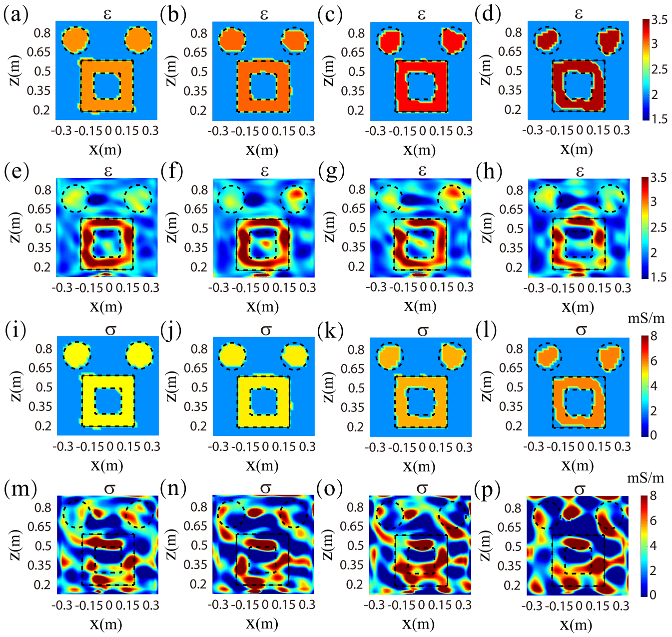

Fig. 9. Reconstructed 2-D xz slices at $y = 0$ m by VBIM-MRF and VBIM for different noise levels. From the first column to the fourth column, the SNRs are 30, 25, 20, and 15 dB, respectively. (a)–(d) Permittivity profiles reconstructed by VBIM-MRF. (e)–(h) Permittivity profiles reconstructed by VBIM. (i)–(l) Conductivity profiles reconstructed by VBIM-MRF. (m)–(p) Conductivity profiles reconstructed by VBIM.

TABLE I

MODEL MISFITS (%) FOR VBIM-MRF AND VBIM WHEN THE SCATTERED FIELD DATA ARE CONTAMINATED BY NOISE WITH DIFFERENT SNRS

Method \ SNR		30 dB	25 dB	20 dB	15 dB
VBIM-MRF	ε	4.30	4.84	6.94	8.91
	σ	11.35	12.58	17.83	22.70
VBIM	ε	10.49	12.22	12.76	14.81
	σ	84.71	101.9	116.7	135.3

6) Antinoise Test: Fig. 9 shows the reconstructed 2-D xz slices by VBIM-MRF and VBIM when the scattered field data are contaminated by the white Gaussian noise. The noise level is defined according to the signal-to-noise ratio (SNR) of power. The model misfits of the reconstruction are listed in Table I. We can see that VBIM-MRF certainly has a stronger antinoise ability than pure VBIM. The reconstructed shapes of the permittivity and conductivity are well kept when VBIM-MRF is employed. This benefits from the constraints of (7) and (8) applied to multiple model parameters simultaneously. For the pure VBIM, there is no constraint for multiple

TABLE II

MIDDLE LAYER BACKGROUND PARAMETERS AND THE TRUE AND RECONSTRUCTED MODEL PARAMETERS OF TWO CUBOIDS

Parameter Object	ε_{11}	ε_{12}	ε_{13}	ε_{22}	ε_{23}	ε_{33}	μ_{11}	μ_{12}	μ_{13}	μ_{22}	μ_{23}	μ_{33}	σ_{11}	σ_{12}	σ_{13}	σ_{22}	σ_{23}	σ_{33}
Middle layer	1.5	0.0	0.0	1.5	0.0	2.0	1.2	0.0	0.0	1.2	0.0	1.8	1.0	0.0	0.0	1.0	0.0	2.0
Top cuboid (true)	2.0	0.5	0.3	1.8	0.3	2.5	1.5	0.2	0.5	1.8	0.2	2.2	2.0	2.0	3.0	5.0	1.0	4.0
Top cuboid (reconstructed)	2.00	0.51	0.28	1.80	0.29	2.51	1.51	0.21	0.53	1.84	0.22	2.23	1.90	2.00	3.00	5.10	0.99	3.90
Bottom cuboid (true)	2.4	0.2	0.6	2.0	0.5	3.2	1.8	0.5	0.2	1.4	0.4	2.7	5.0	4.0	4.0	2.0	3.0	8.0
Bottom cuboid (reconstructed)	2.42	0.21	0.64	2.01	0.51	3.21	1.80	0.49	0.19	1.39	0.38	2.67	5.10	4.10	4.10	2.00	3.00	8.10

Remark: the unit of σ is mS/m.

TABLE III

PROCESS OF DETERMINING THE MRF CLASSIFICATION NUMBER

Iteration#	Classification number	(ratio (%) of cell number, mean of ε', mean of μ', mean of σ')
1	9	(3.21, 2.25, 1.90, 4.12) (0.00, Nan, Nan, Nan) (0.39, 2.14, 1.68, 3.30) (0.75, 2.04, 1.60, 2.88) (5.12, 1.66, 1.38, 1.34) (63.1, 1.66, 1.40, 1.33) (14.7, 1.74, 1.47, 1.58) (5.53, 1.84, 1.53, 1.98) (7.91, 1.98, 1.64, 2.63)
2	8	(1.69, 2.19, 1.85, 3.77) (1.84, 2.15, 1.67, 3.29) (1.73, 2.35, 1.93, 4.54) (8.76, 1.67, 1.38, 1.33) (64.1, 1.66, 1.40, 1.31) (10.3, 1.74, 1.48, 1.59) (6.74, 1.86, 1.54, 2.05) (4.81, 2.01, 1.64, 2.71)
3	7	(2.47, 2.12, 1.78, 3.41) (2.68, 2.08, 1.63, 2.93) (2.52, 2.32, 1.90, 4.35) (8.53, 1.67, 1.38, 1.33) (65.3, 1.66, 1.40, 1.31) (11.1, 1.76, 1.49, 1.65) (7.37, 1.91, 1.58, 2.26)
4	6	(4.81, 2.11, 1.72, 3.22) (2.41, 2.32, 1.90, 4.38) (8.51, 1.67, 1.38, 1.33) (65.5, 1.66, 1.40, 1.31) (11.2, 1.76, 1.49, 1.66) (7.60, 1.92, 1.58, 2.28)
5	5	(4.10, 2.26, 1.85, 4.06) (8.25, 1.67, 1.38, 1.32) (67.6, 1.66, 1.40, 1.32) (12.4, 1.79, 1.51, 1.78) (7.67, 2.00, 1.63, 2.68)
6	4	(0.00, Nan, Nan, Nan) (9.26, 1.61, 1.35, 1.16) (75.1, 1.68, 1.41, 1.38) (15.7, 2.03, 1.67, 2.88)
7	3	(17.9, 1.81, 1.50, 1.86) (73.9, 1.66, 1.40, 1.32) (8.14, 2.16, 1.76, 3.51)

Remark: the unit of σ' is mS/m.

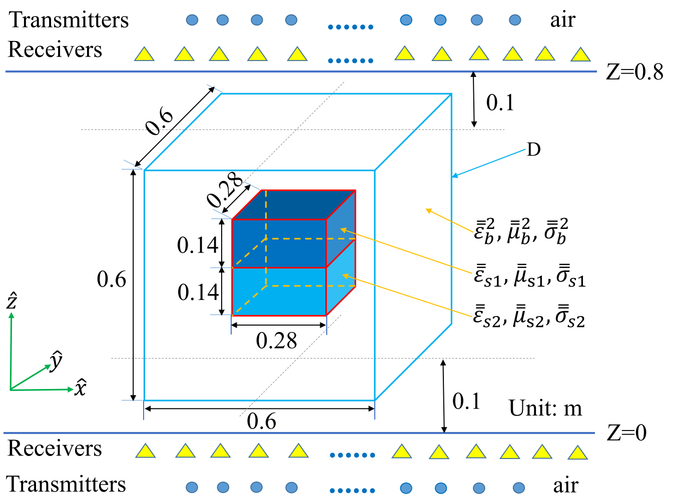

Fig. 10. Configuration of the inversion model with an inhomogeneous cube embedded in the middle layer. The cube includes two cuboids that have the same dimensions of 0.28 m × 0.28 m × 0.14 m.

parameters in the inversion process. The shapes of conductivity are rather bad when noise is added.

B. Inhomogeneous Cube Embedded in the Middle Layer

1) Inversion Model Configuration: In this case, we reconstruct an inhomogeneous cube, including two homogeneous cuboids with the dimensions of 0.28 m × 0.28 m × 0.14 m, as shown in Fig. 10. The middle layer is uniaxial, while two cuboids are fully anisotropic with the symmetrical constitutive tensors. Their true model parameters are listed in Table II. The inversion domain enclosing the scatterer has the dimensions of 0.6 m × 0.6 m × 0.6 m. It is divided into 27 000 cells. The size of each cell is $\Delta x = \Delta y = \Delta z = 0.02$ m. Thus, there are totally 486 000 unknowns to be reconstructed. The 72 transmitters are uniformly placed in two 1.0 m × 1.0 m planes at $z = -0.2$ m and $z = 1.0$ m, respectively. Two operation frequencies 130 and 60 MHz are chosen. The scattered fields are collected by two arrays of 98 receivers that are uniformly located in two 1.5 m × 1.5 m planes at $z = -0.1$ m and $z = 0.9$ m, respectively. Because only the scattered electric fields with 30-dB white Gaussian noise added are used for the inversion, there are totally 84 672 data equations. In addition, only the diagonal elements are used in MRF classification since the values of off-diagonal elements of the model parameter tensors are much smaller than diagonal ones.

2) Determining the Classification Number: It is necessary to determine the number of medium kinds inside the inversion domain if it is unknown. The basic idea is to implement the pure VBIM several times, guess a relatively large number, and iteratively classify the VBIM results according to the assumed or the following adjusted classification number until the results become almost unchanged. For the current example, there are totally three kinds of media in the inversion domain, including the uniaxial background medium. We first implement the pure VBIM five times and obtain the preliminary reconstructed model parameters. Then, we guess that there are nine kinds of media and carry out the MRF classification iteratively. In each iteration, the classification number is decreased by one if the classification satisfies one of the following two conditions: 1) the ratio of the cell number of a certain class with respect to the total cell number in the inversion domain is less than 2% and 2) the differences of the mean values of ε' and μ' between two classes are both less than 0.1, and the difference of the mean values of σ' is less than 0.1 mS/m. The whole process of determining the classification number is shown in Table III. When both 1) and 2) are not satisfied, the iterative MRF classification procedure terminates. One should note that ε',

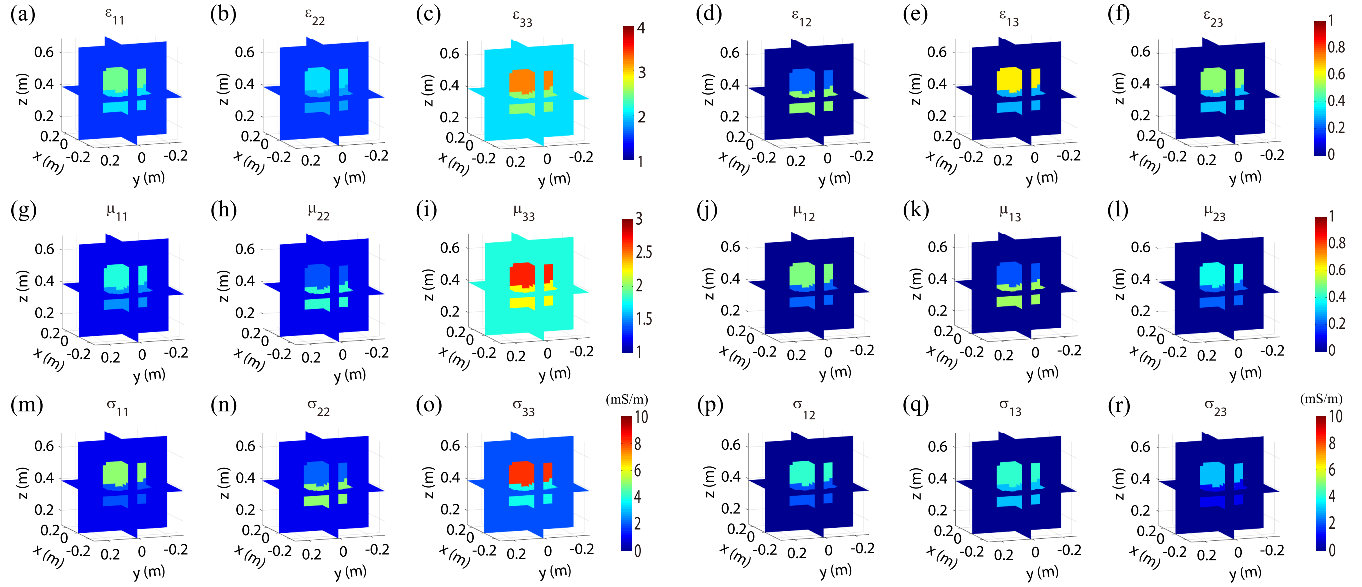

Fig. 11. Reconstructed 3-D profiles of the two connected cuboids by VBIM-MRF. (a)–(f) Relative permittivity. (g)–(l) Relative permeability. (m)–(r) Conductivity.

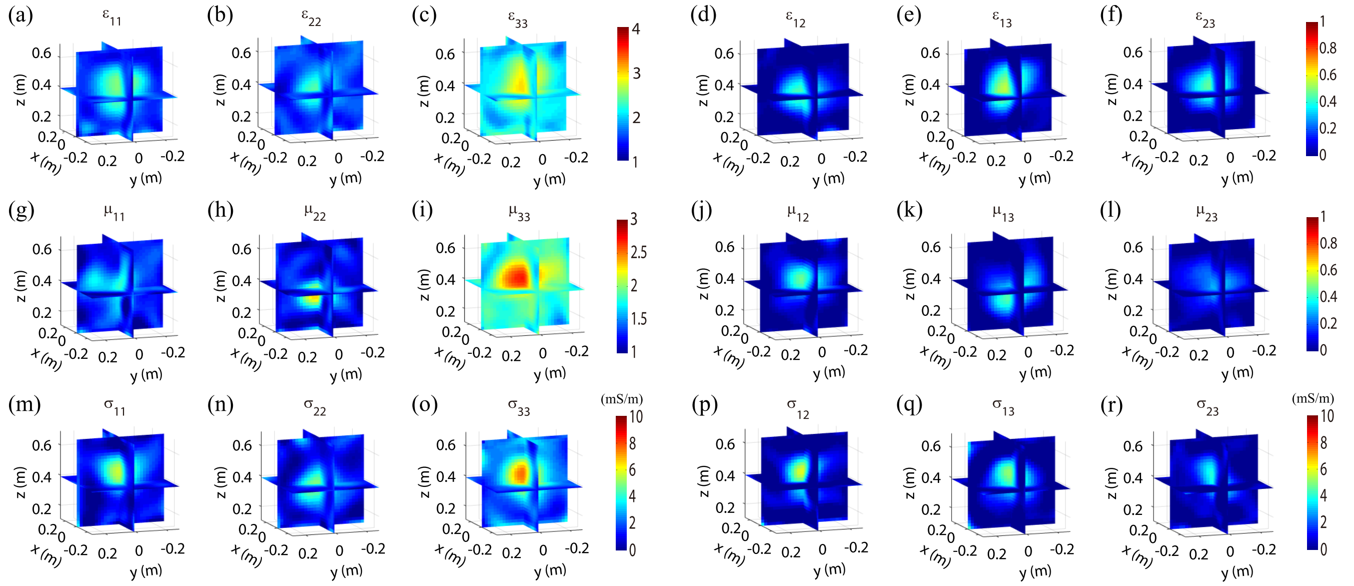

Fig. 12. Reconstructed 3-D profiles of the two connected cuboids by the pure VBIM. (a)–(f) Relative permittivity. (g)–(l) Relative permeability. (m)–(r) Conductivity.

μ' and σ' are defined as

$$\varepsilon' = \frac{\varepsilon_{11} + \varepsilon_{22} + \varepsilon_{33}}{3} \tag{9a}$$

$$\mu' = \frac{\mu_{11} + \mu_{22} + \mu_{33}}{3} \tag{9b}$$

$$\sigma' = \frac{\sigma_{11} + \sigma_{22} + \sigma_{33}}{3} \tag{9c}$$

since we use the mean value of three diagonal parameters to determine the classification number. When the computed classification number is larger than the true classification number in a certain iteration step, the cells of some classes are too few, and the ratio approaches zero. In this situation, the mean values of ε', μ', and σ' are meaningless, and we label them "Nan" in Table III.

3) Full-Wave Inversion of the Anisotropic Scatterer by VBIM-MRF: Based on the obtained classification number, we perform the full-wave inversion using the VBIM-MRF. The reconstructed 3-D profiles are shown in Fig. 11, and the model parameters are listed in Table II. We can see that the hybrid method also shows good performance for fully anisotropic scatterers with 18 unknowns even when the scattered field data are contaminated by 30-dB noise. We also use pure VBIM to reconstruct the same anisotropic scatterer, and the results are shown in Fig. 12. We can see that only the approximate location of the scatterer is found. The boundary between two different subscatterers cannot be located by VBIM.

IV. CONCLUSION AND DISCUSSION

In this article, the traditional full-wave variational BIM is optimized by the MRF model. The discretized cells in the inversion domain are classified according to the reconstructed model parameter values, and partial "background" cells are removed and partial "scatterer" cells merged in each iteration. As a result, the discretized data equations gradually contract. Both the time and memory costs are significantly reduced compared with the cost of pure VBIM.

Two model parameters, including the permittivity and the conductivity, are reconstructed by VBIM-MRF in the first numerical example. The intermediate inversion results in each VBIM iteration clearly illustrate the facilitative effect of the MRF model, and the final reconstructed results show the feasibility and effectiveness of the hybrid method. The comparisons between the hybrid and the traditional methods show that the VBIM-MRF outperforms the pure VBIM for the inversion precision, implementation efficiency, and the antinoise ability. In the second numerical example, it is demonstrated that the proposed hybrid method is also capable of inverting for multiple parameters of fully anisotropic inhomogeneous scatterers even when the measured data are contaminated by noise. In addition, an iterative classification method is proposed to compute the number of medium kind if it is unknown before the full-wave inversion.

One may raise the question regarding the applicability of the proposed VBIM-MRF for multiple homogeneous scatterers or subscatterers embedded in the inversion domain. Because the MRF model is based on the statistical results of a lot of discretized cells that share the same true model parameters, only when each homogeneous scatterer or subscatterer takes enough discretized cells, the parameter estimation and classification can be performed. Therefore, the electrical sizes of the scatterers will be rather large if a large number of homogeneous scatterers or subscatterers are included in the inversion domain. In this situation, the iteration of VBIM will fail to converge due to the strong scattering. Another disadvantage of the proposed hybrid method is that its efficiency and reliability depend on the thresholds $th1$, $th2$, and $th3$ in (7) and (8). Inappropriate values of these parameters may cause unstable iterations of VBIM or even the convergence failure.

Future work will be focused on two aspects. First, reconstruct scatterers including arbitrary inhomogeneous media or even continuously varying media for which the proposed method will fail. One possible solution for such EM scattering scenarios is adding some gradient constraints to the unknown model parameters in the cost function and to adopt other auxiliary statistical methods. Second, validate the hybrid method using the laboratory experimental data. However, this will be left as future work.

REFERENCES

[1] G. Wang, X.-G. Xia, and V. C. Chen, "Radar imaging of moving targets in foliage using multifrequency multiaperture polarimetric SAR," *IEEE Trans. Geosci. Remote Sens.*, vol. 41, no. 8, pp. 1755–1764, Aug. 2003.

[2] K. D. Paulsen, S. P. Poplack, D. Li, M. W. Fanning, and P. M. Meaney, "A clinical prototype for active microwave imaging of the breast," *IEEE Trans. Microw. Theory Techn.*, vol. 48, no. 11, pp. 1841–1853, Nov. 2000.

[3] F. García-Rial, D. Montesano, I. Gómez, C. Callejero, F. Bazus, and J. Grajal, "Combining commercially available active and passive sensors into a millimeter-wave imager for concealed weapon detection," *IEEE Trans. Microw. Theory Techn.*, vol. 67, no. 3, pp. 1167–1183, Mar. 2019.

[4] S. Maiti, S. K. Patra, and A. Bhattacharya, "A modified plane wave model for fast and accurate characterization of layered media," *IEEE Trans. Microw. Theory Techn.*, vol. 65, no. 9, pp. 3492–3502, Sep. 2017.

[5] G. Li, H. Cai, and C.-F. Li, "Alternating joint inversion of controlled-source electromagnetic and seismic data using the joint total variation constraint," *IEEE Trans. Geosci. Remote Sens.*, vol. 57, no. 8, pp. 5914–5922, Aug. 2019.

[6] S. Yang, J. Wang, J. Zhou, T. Zhu, and H. Wang, "An efficient algorithm of both Fréchet derivative and inversion of MCIL data in a deviated well in a horizontally layered TI formation based on TLM modeling," *IEEE Trans. Geosci. Remote Sens.*, vol. 52, no. 11, pp. 6911–6923, Nov. 2014.

[7] K. Xu, Y. Zhong, X. Chen, and D. Lesselier, "A fast integral equation-based method for solving electromagnetic inverse scattering problems with inhomogeneous background," *IEEE Trans. Antennas Propag.*, vol. 66, no. 8, pp. 4228–4239, Aug. 2018.

[8] H. Liu, Z. Long, F. Han, G. Fang, and Q. H. Liu, "Frequency-domain reverse-time migration of ground penetrating radar based on layered medium Green's functions," *IEEE J. Sel. Topics Appl. Earth Observ. Remote Sens.*, vol. 11, no. 8, pp. 2957–2965, Aug. 2018.

[9] D. Colton, H. Haddar, and M. Piana, "The linear sampling method in inverse electromagnetic scattering theory," *Inverse Problems*, vol. 19, no. 6, pp. S105–S137, Nov. 2003.

[10] I. Catapano, L. Crocco, and T. Isernia, "OnSimple methodsfor shape reconstruction of unknown scatterers," *IEEE Trans. Antennas Propag.*, vol. 55, no. 5, pp. 1431–1436, May 2007.

[11] K. Ito, B. Jin, and J. Zou, "A direct sampling method to an inverse medium scattering problem," *Inverse Problems*, vol. 28, no. 2, Jan. 2012, Art. no. 025003.

[12] M. T. Bevacqua, T. Isernia, R. Palmeri, M. N. Akıncı, and L. Crocco, "Physical insight unveils new imaging capabilities of orthogonality sampling method," *IEEE Trans. Antennas Propag.*, vol. 68, no. 5, pp. 4014–4021, May 2020.

[13] L. Ding, X. L. Deán-Ben, and D. Razansky, "Real-time model-based inversion in cross-sectional optoacoustic tomography," *IEEE Trans. Med. Imag.*, vol. 35, no. 8, pp. 1883–1891, Aug. 2016.

[14] L. Ke, F. Cao, and Q. Du, "An improved back-projection algorithm for magnetic induction tomography based on magnetic field lines," in *Proc. 7th Int. Conf. Biomed. Eng. Informat.*, Oct. 2014, pp. 32–36.

[15] T. M. Habashy, R. W. Groom, and B. R. Spies, "Beyond the born and Rytov approximations: A nonlinear approach to electromagnetic scattering," *J. Geophys. Res. Solid Earth*, vol. 98, no. B2, pp. 1759–1775, Feb. 1993.

[16] R. Palmeri, M. T. Bevacqua, L. Crocco, T. Isernia, and L. Di Donato, "Microwave imaging via distorted iterated virtual experiments," *IEEE Trans. Antennas Propag.*, vol. 65, no. 2, pp. 829–838, Feb. 2017.

[17] Y. M. Wang and W. C. Chew, "An iterative solution of the two-dimensional electromagnetic inverse scattering problem," *Int. J. Imag. Syst. Technol.*, vol. 1, no. 1, pp. 100–108, 1989.

[18] F. Li, Q. H. Liu, and L.-P. Song, "Three-dimensional reconstruction of objects buried in layered media using born and distorted born iterative methods," *IEEE Geosci. Remote Sens. Lett.*, vol. 1, no. 2, pp. 107–111, Apr. 2004.

[19] N. Zaiping, Y. Feng, Z. Yanwen, and Z. Yerong, "Variational born iteration method and its applications to hybrid inversion," *IEEE Trans. Geosci. Remote Sens.*, vol. 38, no. 4, pp. 1709–1715, Jul. 2000.

[20] P. M. Van Den Berg and R. E. Kleinman, "A contrast source inversion method," *Inverse Problems*, vol. 13, no. 6, pp. 1607–1620, Dec. 1997.

[21] X. Chen, "Subspace-based optimization method for solving inverse-scattering problems," *IEEE Trans. Geosci. Remote Sens.*, vol. 48, no. 1, pp. 42–49, Jan. 2010.

[22] Z. Wei and X. Chen, "Deep-learning schemes for full-wave nonlinear inverse scattering problems," *IEEE Trans. Geosci. Remote Sens.*, vol. 57, no. 4, pp. 1849–1860, Apr. 2019.

[23] L. Li, L. G. Wang, F. L. Teixeira, C. Liu, A. Nehorai, and T. J. Cui, "DeepNIS: Deep neural network for nonlinear electromagnetic inverse scattering," *IEEE Trans. Antennas Propag.*, vol. 67, no. 3, pp. 1819–1825, Mar. 2019.

[24] Z. Kato and T.-C. Pong, "A Markov random field image segmentation model for color textured images," *Image Vis. Comput.*, vol. 24, no. 10, pp. 1103–1114, Oct. 2006.

[25] S. Caorsi, G. L. Gragnani, S. Medicina, M. Pastorino, and G. Zunino, "Microwave imaging based on a Markov random field model," *IEEE Trans. Antennas Propag.*, vol. 42, no. 3, pp. 293–303, Mar. 1994.

[26] L. Gharsalli, H. Ayasso, B. Duchene, and A. Mohammad-Djafari, "Inverse scattering in a Bayesian framework: Application to microwave imaging for breast cancer detection," *Inverse Problems*, vol. 30, no. 11, pp. 1–26, 2014.

[27] L. Poli, G. Oliveri, F. Viani, and A. Massa, "MT—BCS-based microwave imaging approach through minimum-norm current expansion," *IEEE Trans. Antennas Propag.*, vol. 61, no. 9, pp. 4722–4732, Sep. 2013.

[28] G. Oliveri, M. Salucci, N. Anselmi, and A. Massa, "Compressive sensing as applied to inverse problems for imaging: Theory, applications, current trends, and open Challenges.," *IEEE Antennas Propag. Mag.*, vol. 59, no. 5, pp. 34–46, Oct. 2017.

[29] M. T. Bevacqua, L. Crocco, L. Di Donato, and T. Isernia, "Microwave imaging of nonweak targets via compressive sensing and virtual experiments," *IEEE Antennas Wireless Propag. Lett.*, vol. 14, pp. 1035–1038, 2015.

[30] K. A. Michalski and J. R. Mosig, "Multilayered media Green's functions in integral equation formulations," *IEEE Trans. Antennas Propag.*, vol. 45, no. 3, pp. 508–519, Mar. 1997.

[31] P. Zwamborn and P. M. van den Berg, "The three dimensional weak form of the conjugate gradient FFT method for solving scattering problems," *IEEE Trans. Microw. Theory Techn.*, vol. 40, no. 9, pp. 1757–1766, Sep. 1992.

[32] F. Han, J. Zhuo, N. Liu, Y. Liu, H. Liu, and Q. H. Liu, "Fast solution of electromagnetic scattering for 3-D inhomogeneous anisotropic objects embedded in layered uniaxial media by the BCGS-FFT method," *IEEE Trans. Antennas Propag.*, vol. 67, no. 3, pp. 1748–1759, Mar. 2019.

[33] Y. Chen, P. Wen, F. Han, N. Liu, H. Liu, and Q. H. Liu, "Three-dimensional reconstruction of objects embedded in spherically layered media using variational born iterative method," *IEEE Geosci. Remote Sens. Lett.*, vol. 14, no. 7, pp. 1037–1041, Jul. 2017.

[34] W. Zhang and Q. H. Liu, "Three-dimensional scattering and inverse scattering from objects with simultaneous permittivity and permeability contrasts," *IEEE Trans. Geosci. Remote Sens.*, vol. 53, no. 1, pp. 429–439, Jan. 2015.

[35] K. Held, E. R. Kops, B. J. Krause, W. M. Wells, R. Kikinis, and H.-W. Müller-Gärtner, "Markov random field segmentation of brain MR images," *IEEE Trans. Med. Imag.*, vol. 16, no. 6, pp. 878–886, Dec. 1997.

[36] T. Lan, N. Liu, F. Han, and Q. H. Liu, "Joint petrophysical and structural inversion of electromagnetic and seismic data based on volume integral equation method," *IEEE Trans. Geosci. Remote Sens.*, vol. 57, no. 4, pp. 2075–2086, Apr. 2019.

[37] J. Besag, "Spatial interaction and the statistical analysis of lattice systems," *J. Roy. Statist. Soc. B*, vol. 36, no. 2, pp. 192–236, 1974.

[38] S. Geman and D. Geman, "Stochastic relaxation, gibbs distributions, and the Bayesian restoration of images," *IEEE Trans. Pattern Anal. Mach. Intell.*, vols. PAMI-6, no. 6, pp. 721–741, Nov. 1984.

[39] T. Szirányi, J. Zerubia, L. Czúni, D. Geldreich, and Z. Kato, "Image segmentation using Markov random field model in fully parallel cellular network architectures," *Real-Time Imag.*, vol. 6, no. 3, pp. 195–211, Jun. 2000.

[40] A. H. S. Solberg, T. Taxt, and A. K. Jain, "A Markov random field model for classification of multisource satellite imagery," *IEEE Trans. Geosci. Remote Sens.*, vol. 34, no. 1, pp. 100–113, Jan. 1996.

[41] A. Tarantola, Ed., *Inverse Problem Theory and Methods for Model Parameter Estimation*. Philadelphia, PA, USA: SIAM, 2005.

[42] A. Abubaker and P. M. Van Den Berg, "Total variation as a multiplicative constraint for solving inverse problems," *IEEE Trans. Image Process.*, vol. 10, no. 9, pp. 1384–1392, Sep. 2001.

[43] S. Caorsi, M. Donelli, D. Franceschini, and A. Massa, "A new methodology based on an iterative multiscaling for microwave imaging," *IEEE Trans. Microw. Theory Techn.*, vol. 51, no. 4, pp. 1162–1173, Apr. 2003.

[44] M. Salucci, G. Oliveri, and A. Massa, "GPR prospecting through an inverse-scattering frequency-hopping multifocusing approach," *IEEE Trans. Geosci. Remote Sens.*, vol. 53, no. 12, pp. 6573–6592, Dec. 2015.

[45] P. Chiappinelli, L. Crocco, T. Isernia, and V. Pascazio, "Multiresolution techniques in microwave tomography and subsurface sensing," in *Proc. Geosci. Remote Sens. Symp.*, 1999, pp. 2516–2518.

[46] X. Huang, J. Li, Y. Chen, F. Han, and Q. H. Liu, "Hybrid electromagnetic inversion of 3-D irregular scatterers embedded in layered media by VBIM and MET," *IEEE Trans. Antennas Propag.*, to be published.

[47] J. Li, Y. Chen, J. Zhuo, F. Han, Y. Liu, and Q. H. Liu, "3-D voxel-based reconstruction of multiple objects buried in layered media by VBIM hybridized with unsupervised machine learning," *IEEE Trans. Antennas Propag.*, to be published.

Yanjin Chen received the B.S. degree in mechanical and electronic engineering from the Hainan University of China, Hainan, China, in 2017. He is currently pursuing the Ph.D. degree at Xiamen University, Xiamen, China.

His current research interest is applying the machine learning techniques to electromagnetic inverse scattering problems.

Jiawen Li received the B.S. degree in electronic science and technology from the Wuhan University of Technology of China, Wuhan, China, in 2011. He is currently pursuing the Ph.D. degree at Xiamen University, Xiamen, China.

His research interests include electromagnetic scattering and inverse scattering in complex media and the full-wave inversion of anisotropic targets.

Jianliang Zhuo received the B.S. degree in communication engineering and business administration and the M.S. degree in communication and information system from the University of Electronic Science and Technology of China, Chengdu, China, in 2007 and 2011, respectively, and the Ph.D. degree in physical electronics from Xiamen University, Xiamen, China, in 2018.

His research interests include fast forward solvers in electromagnetics and inverse scattering methods for microelectronics and RF systems.

Feng Han (Senior Member, IEEE) received the B.S. degree in electronic science from Beijing Normal University, Beijing, China, in 2003, the M.S. degree in geophysics from Peking University, Beijing, in 2006, and the Ph.D. degree in electrical engineering from Duke University, Durham, NC, USA, in 2011.

He is currently an Assistant Professor with the Institute of Electromagnetics and Acoustics, Xiamen University, Xiamen, China. His research interests include ionosphere remote sensing by radio atmospherics, electromagnetic full-wave inversion by integral equations, reverse time migration image, and the design of an electromagnetic detection system.

Qing Huo Liu (Fellow, IEEE) received the B.S. and M.S. degrees in physics from Xiamen University, Xiamen, China, and the Ph.D. degree in electrical engineering from the University of Illinois at Urbana-Champaign, Champaign, IL, USA.

From September 1986 to December 1988, he was a Research Assistant with the Electromagnetics Laboratory, University of Illinois at Urbana-Champaign, where he was a Post-Doctoral Research Associate from January 1989 to February 1990. He was a Research Scientist and the Program Leader with Schlumberger-Doll Research, Ridgefield, CT, USA, from 1990 to 1995. From 1996 to May 1999, he was an Associate Professor with New Mexico State University, Las Cruces, NM, USA. Since June 1999, he has been with Duke University, Durham, NC, USA, where he is currently a Professor of electrical and computer engineering. He has also been the Founder and Chairman of Wave Computation Technologies, Inc., Durham, NC, USA, since 2005. His research interests include computational electromagnetics and acoustics, inverse problems, and their application in nanophotonics, geophysics, biomedical imaging, and electronic packaging. He has published widely in these areas.